Forecast-Based MPC of a Hydrogen-Integrated Multi-Energy System with Dynamic Building Modeling

Samuel Peifer*, Peter Renze

Institute for Energy Technology and Energy Economics, University of Applied Science, Albert-Einstein-Allee 55, 89081 Ulm, Germany; *samuel.peifer@thu.de

SNE 36(1), 2026, 45-53, DOI: 10.11128/sne.36.tn.10767
Selected ASIM GMMS/STS 2025 Postconf. Publ.: 2025-10-22
Revised English: 26-01-2026; Accepted: 2026-02-15
SNE - Simulation Notes Europe, ARGESIM Publisher Vienna
ISSN Print 2305-9974, Online 2306-0271, www.sne-journal.org

Abstract. This paper presents a system-level modeling and control framework for a small-scale power-to-X (P-t-X) facility coupled with a dynamic building model. The considered system configuration and parameterization are based on a real-world energy research facility at the Technische Hochschule Ulm. A forecast-based model predictive control (MPC) strategy is compared to a conventional rule-based approach. The MPC is formulated as a mixed-integer linear program (MILP), integrates time series forecasts, and limits daily start events of key conversion units via an ε-constraint. Results indicate the potential of predictive operation to improve self-sufficiency and self-consumption while respecting operational and building comfort constraints.

Introduction

Hydrogen produced from renewable electricity is expected to play a key role in a future climate-neutral energy system [1]. The fluctuating nature of renewable generation leads to temporal mismatches between supply and demand, requiring flexible storage and operation strategies. In this context, the combination of hydrogen and battery energy storage is a promising solution [2].

Sector coupling and waste heat utilization further increase system flexibility, particularly when power-to-X (P-t-X) systems are integrated with building thermal dynamics.

However, suitable operation strategies remain challenging, especially under operational constraints such as limited start events of conversion units.

This paper presents a system-level modeling and control framework for a small-scale P-t-X facility coupled with a dynamic building model. A rule-based operation strategy is compared with a forecast-based model predictive control (MPC) approach formulated as a mixed-integer linear program (MILP).

The MPC integrates time series forecasts and limits electrolyzer and gas turbine starts via an ε-constraint, aiming to improve self-sufficiency and self-consumption while respecting operational and comfort constraints.

The remainder of the paper is structured as follows: Section 1 introduces the system, Section 2 the data basis, and Section 3 the building model. Section 5 presents the MPC formulation, followed by results and conclusions.

1 System Description

The considered system is an electrically and thermally integrated power-to-gas (PtG) and power-to-power (PtP) infrastructure coupled to a building energy system.

As shown in Figure 1, electrical energy is supplied by photovoltaic generation and the grid and consumed by the building load, an electrolyzer, a hydrogen driven gas turbine, and a battery energy storage system (BESS).

Electrical surpluses are converted to hydrogen via the electrolyzer and stored in a hydrogen energy storage system (HESS), while deficits are covered by reconversion through the gas turbine or grid import.

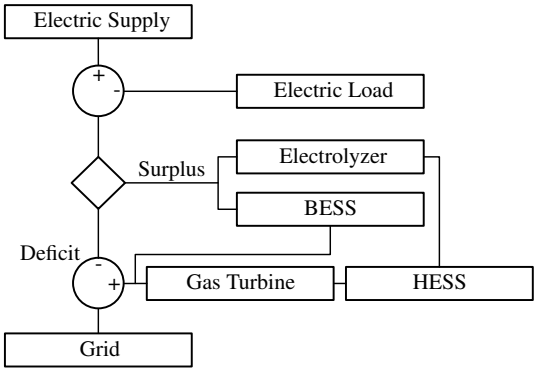

Figure 1: System model of the P-t-G / P-t-P infrastructure [3].

Thermal integration is realized by waste heat recovery from the gas turbine and an electrically driven heat pump (Figure 2).

Thermal energy is used to supply the building demand or charge a sensible thermal energy storage (TES), which provides additional flexibility for balancing heat supply and demand.

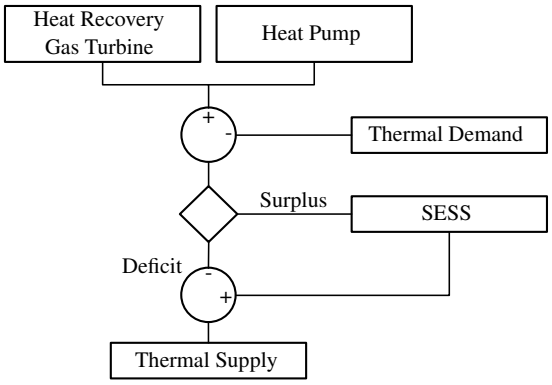

Figure 2: System model of the thermal integration and heat recovery [3].

The building thermal demand is modeled dynamically using a 3R2C grey-box model (Section 3), providing time-varying heating and cooling demands for the energy management system.

The resulting multi-energy system enables flexible coupling of electrical, thermal, and hydrogen energy flows and forms the basis for the optimization-based operation strategy.

2 Data and Preprocessing

2.1 Data sources and signals

The data set comprises time series of photovoltaic power generation, electrical load, thermal demand, and meteorological variables, including ambient temperature, global horizontal irradiance, wind speed, and wind direction.

The data cover the period 2023–2025 and are obtained from the building management system of Technische Hochschule Ulm (TH Ulm), University of Applied Sciences.

Figure 3 illustrates exemplary annual meteorological time series, highlighting both seasonal patterns and short-term variability relevant for load forecasting and building thermal modeling.

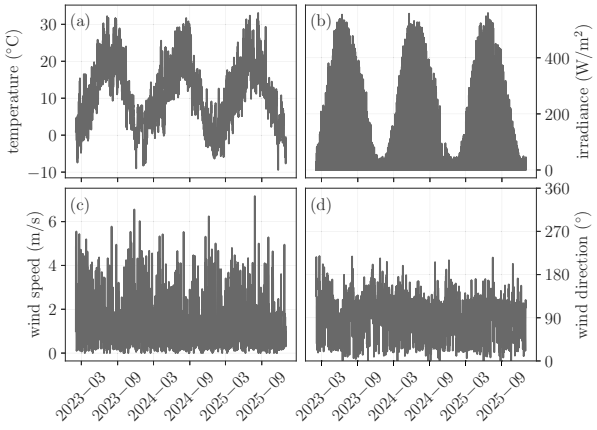

Figure 3: Exemplary annual time series of meteorological variables (2023–2025).

Monthly aggregated energy quantities of photovoltaic generation, electrical load, and thermal demand are shown in Fig. 4, highlighting their pronounced seasonal mismatch.

2.2 Temporal resolution and alignment

All signals are aligned to a common hourly time grid. Higher-resolution data are aggregated in an energy-conserving manner, while lower-resolution data are upsampled using zero-order hold.

Time stamps are converted to a consistent time zone, and short data gaps are filled by interpolation.

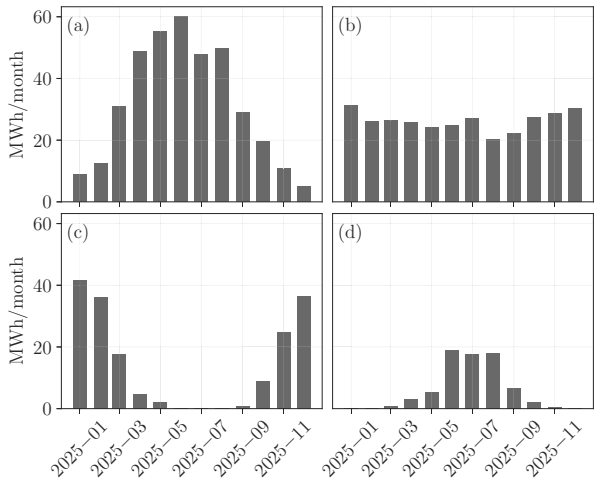

Figure 4: Monthly aggregated energy quantities of photovoltaic generation (a), electrical load (b), and thermal demand (c,d) for the period 2023–2025.

3 Building Model and Calibration (3R2C + IPOPT)

3.1 Grey-box model structure

The building thermal behavior is modeled using a ventilation-aware 3R2C grey-box model following [4]. Two thermal states are considered: the indoor air temperature T_{in} and the effective envelope temperature T_{e}.

The model is driven by ambient temperature T_{a}, solar gains Q_{s}, and HVAC thermal input Q_{h}, allowing the separation of fast indoor air dynamics and slower envelope dynamics.

3.2 Continuous-time 3R2C dynamics

The continuous-time dynamics of the 3R2C model are given by

$$C_{\text{in}}\frac{dT_{\text{in}}}{dt} = \frac{T_{\text{e}}-T_{\text{in}}}{R_{\text{in,e}}} + \frac{T_{\text{a}}-T_{\text{in}}}{R_{\text{in,a}}} + f_{\text{h}}Q_{\text{h}} + A_{\text{in}}Q_{\text{s}}, \tag{1}$$

$$C_{\text{e}}\frac{dT_{\text{e}}}{dt} = \frac{T_{\text{in}}-T_{\text{e}}}{R_{\text{in,e}}} + \frac{T_{\text{a}}-T_{\text{e}}}{R_{\text{e,a}}} + (1-f_{\text{h}})Q_{\text{h}} + A_{\text{e}}Q_{\text{s}}. \tag{2}$$

For the discretization a discrete time step Δt is used and the model is transformed into the state-space form

$$\mathbf{T}_{k+1} = \mathbf{A}_d(\theta)\,\mathbf{T}_k + \mathbf{B}_d(\theta)\,\mathbf{u}_k, \tag{3}$$

which is embedded as linear constraints in the MPC after calibration.

3.3 Parameter estimation as NLP (IPOPT)

The parameter vector

$$\theta = \{R_{\text{in,e}}, R_{\text{in,a}}, R_{\text{e,a}}, C_{\text{in}}, C_{\text{e}}, A_{\text{in}}, A_{\text{e}}, f_{\text{h}}, T_{\text{e,0}}\}$$

is identified by solving a nonlinear program subject to the discretized model dynamics. Calibration minimizes a weighted sum of the indoor air temperature tracking error

$$J_T(\theta) = \frac{1}{N}\sum_{k=1}^{N}\left(T_{\text{in},k}(\theta) - T_{\text{in},k}^{\text{meas}}\right)^2, \tag{4}$$

In contrast to the method proposed by Panagi et al. [4], we additionally include the normalized deviation between simulated and measured monthly thermal energy demand,

$$J_E(\theta) = \frac{1}{12}\sum_{m=1}^{12}\left(\frac{E_m^{\text{sim}}(\theta) - E_m^{\text{meas}}}{\max(\varepsilon_E, E_m^{\text{meas}})}\right)^2. \tag{5}$$

Both objectives are combined as

$$\min_{\theta} J(\theta) = w_T J_T(\theta) + w_E J_E(\theta), \tag{6}$$

subject to the discretized model equations and parameter bounds.

3.4 Model evaluation

Model performance is assessed on both the calibration data set and an independent test period.

Figure 5 shows the indoor air temperature during the best-fitting calibration window, illustrating that the identified parameters accurately reproduce the short-term thermal dynamics of the building.

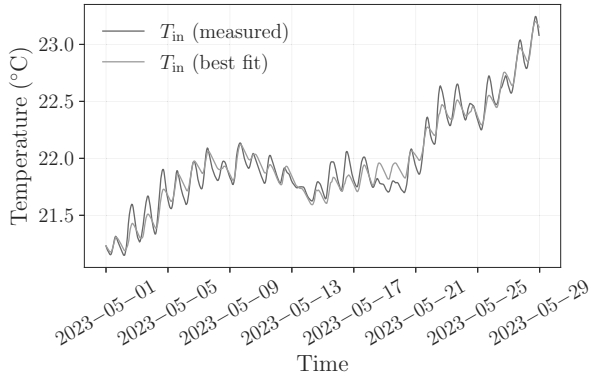

Figure 5: Measured and simulated indoor air temperature during the calibration window (best training fit).

Generalization capability is evaluated on the unseen test year 2025.

Figure 6 compares simulated and measured monthly thermal energy demand, demonstrating that the model reproduces the aggregated thermal energy balance over an annual horizon with sufficient accuracy for predictive control applications.

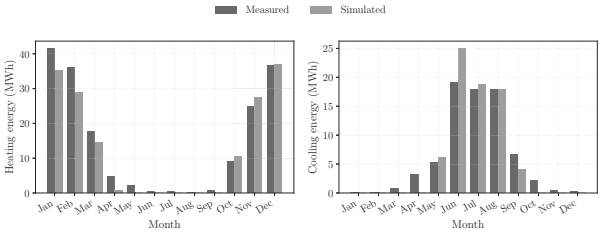

Figure 6: Comparison of measured and simulated monthly thermal energy demand for the test year 2025.

3.5 Thermal Component Modelling (1R1C)

Thermal components such as the electrolyzer and gas turbine are represented by a first-order resistance–capacitance (1R1C) model following [5].

The discrete-time temperature dynamics are given by the formula

$$T_{k+1} = T_k + \frac{\Delta t}{C}\left(Q_{\text{in},k} - \frac{T_k - T_{\text{a},k}}{R}\right), \qquad (7)$$

and are consistently embedded into the MPC formulation.

Model parameters are calibrated such that a warm-up period of 15 min is required before production starts. The electrolyzer and gas turbine efficiencies are modeled as load-dependent and represented by a piecewise linear approximation using SOS2 constraints [6].

4 Forecasting Models

4.1 Role in MPC

Short-term forecasts of exogenous signals are required for predictive control in multi-energy systems, as photovoltaic generation, electrical load, and ambient temperature directly affect storage scheduling and unit commitment decisions.

Following [7], data-driven forecasting models are therefore integrated into the MPC framework to provide horizon-wise predictions over the control horizon.

Multivariate Long Short-Term Memory (LSTM) networks are employed due to their ability to capture diurnal patterns and temporal dependencies in energy and weather-related time series [8].

Separate models are trained for irradiance, PV power, electrical load, and ambient temperature to account for their differing dynamics.

4.2 Model setup and training

All forecasting models are trained on synchronized hourly data from 2023–2024 using a strict chronological split, while the year 2025 is reserved for out-of-sample evaluation and rolling MPC operation.

Multichannel input sequences of length $L = 24\,\text{h}$ are used and normalized using Min–Max scaling. Temporal ordering is preserved by disabling shuffling.

Lightweight, target-specific LSTM architectures are employed. Linear output activation is used for temperature forecasting, whereas softplus activation is applied to power-related targets to enforce non-negativity.

A seasonal naive forecast with a 24 h lag serves as a baseline. The global training configuration and target-specific network settings are summarized in Tables 1 and 2.

Setting	Value
Train/Val window	2023-02-01 .. 2024-12-31
Chronological split	Train: 90%, Val: 10% (tail)
Test window	2025-01-01 .. 2025-12-31
Rolling export (MPC)	2025-01-01 .. 2025-12-31
Input sequence length (L)	24 h
Forecast horizon (H)	24 h
Batch size	128
Epochs	200
Scaler	Min–Max (0..1)
Multichannel inputs	True
Shuffle training blocks	False
Seasonal naive baseline	24 h

Table 1: Global configuration for all LSTM forecast models.

Target	LSTM units	Output activation
T_{air}	64	linear
PV power	32	softplus
Load	32	softplus
Irradiance	32	softplus

Table 2: Target-specific LSTM output configuration. Softplus enforces non-negativity for power and irradiance targets.

4.3 Forecast accuracy

Forecast accuracy is evaluated on the full test year 2025 using standard error metrics. Table 3 compares the best-performing LSTM models with a seasonal naive baseline. Across all targets, the LSTM models substantially reduce prediction errors, particularly for electrical load and PV power, which are most relevant for MPC decision-making.

Target	Model	RMSE	MAE	R^2
(G_h)	SN	99.56 W/m^2	44.27 W/m^2	0.762
	LSTM	**79.48 W/m^2**	45.91 W/m^2	**0.848**
(P_{PV})	SN	35.73 kW	15.74 kW	0.743
	LSTM	**28.28 kW**	15.45 kW	**0.839**
(P_{load})	SN	15.80 kW	9.12 kW	0.311
	LSTM	**7.91 kW**	5.54 kW	**0.827**
(T_{air})	SN	3.20 °C	2.43 °C	0.843
	LSTM	**2.43 °C**	1.81 °C	**0.909**

Table 3: Forecast accuracy on the test year 2025. SN denotes a seasonal naive baseline (24 h). LSTM uses the full feature set.

5 MPC formulation (MILP with ε-constraint on starts)

5.1 Decision variables

Over the prediction horizon $k = 1,\dots,H$, the MPC optimizes electrical and thermal power flows, storage states, and binary commitment variables.

The decision vector $\mathbf{x}$ comprises:

(i) electrical grid exchange, battery charge/discharge, electrolyzer power, and gas turbine electric output;

(ii) thermal grid exchange, TES charge/discharge, gas turbine heat, and heat pump output;

(iii) storage states of BESS, HESS, and TES;

(iv) building states (indoor and envelope temperatures); and

(v) binary variables enforcing unit commitment and mutually exclusive operating modes.

5.2 Objective and MILP

The primary objective minimizes weighted electrical and thermal grid interactions:

$$J_1 = \sum_{k=1}^{H} \Big(w_{\text{imp}} \big(P^k_{\text{grid,imp}} + Q^k_{\text{hot,imp}} + Q^k_{\text{cold,imp}} \big) + w_{\text{exp}} \big(P^k_{\text{grid,exp}} + Q^k_{\text{hot,exp}} + Q^k_{\text{cold,exp}} \big) \Big) \Delta t. \tag{8}$$

with $w_{\text{imp}} > 0$ and typically $w_{\text{exp}} \ll w_{\text{imp}}$.

At each MPC step, the following mixed-integer linear program is solved:

$$\min_{\mathbf{x}} \quad J_1(\mathbf{x}) \tag{9}$$

$$\text{s.t.} \quad J^{\text{ely}}_{\text{start}}(\mathbf{x}) \le \varepsilon_{\text{ely}}, \qquad J^{\text{gt}}_{\text{start}}(\mathbf{x}) \le \varepsilon_{\text{gt}}, \tag{10}$$

$$\mathbf{f}_{\text{el}}(\mathbf{x},\mathbf{d}) = \mathbf{0}, \qquad \mathbf{f}_{\text{th}}(\mathbf{x},\mathbf{d}) = \mathbf{0}, \tag{11}$$

$$\mathbf{g}_{\text{stor}}(\mathbf{x}) \le \mathbf{0}, \qquad \mathbf{g}_{\text{uc}}(\mathbf{x}) \le \mathbf{0}, \tag{12}$$

$$\mathbf{f}_{\text{bld}}(\mathbf{x},\mathbf{d}) = \mathbf{0}, \tag{13}$$

where $\mathbf{d}$ collects exogenous forecasts (PV generation, electrical demand, weather).

The resulting MILP is implemented in PYTHON using the PYOMO modeling framework and solved with Gurobi [9].

At each MPC step, the MILP is solved to obtain an optimal control sequence, of which only the first control action is applied to the simulation model in a receding-horizon fashion.

5.3 ε-constraint on start events (Ely/GT)

To limit start events, the electrolyzer (Ely) and gas turbine (GT) are explicitly constrained. Binary start indicators detect off–on transitions:

$$\delta^k_{\mathrm{u,start}} \geq \delta^k_{\mathrm{u}} - \delta^{k-1}_{\mathrm{u}}, \qquad \mathrm{u} \in \{\mathrm{ely}, \mathrm{gt}\}, \quad \forall k \geq 1, \tag{14}$$

with known initial states δ^0_{u} from the previous MPC step. The total number of starts over the horizon is

$$J^{\mathrm{u}}_{\mathrm{start}} = \sum_{k=1}^{H} \delta^k_{\mathrm{u,start}}, \qquad \mathrm{u} \in \{\mathrm{ely}, \mathrm{gt}\}, \tag{15}$$

and constrained as

$$J^{\mathrm{ely}}_{\mathrm{start}} \leq \varepsilon_{\mathrm{ely}}, \qquad J^{\mathrm{gt}}_{\mathrm{start}} \leq \varepsilon_{\mathrm{gt}}, \tag{16}$$

with $\varepsilon_{\mathrm{ely}} = \varepsilon_{\mathrm{gt}} = 3$ in this study.

5.4 Constraints

Electrical power balance.

$$P^k_{\mathrm{pv}} + P^k_{\mathrm{gt,el}} + P^k_{\mathrm{bat,dis}} + P^k_{\mathrm{grid,imp}} = P^k_{\mathrm{load}} + P^k_{\mathrm{ely,el}} + P^k_{\mathrm{preheat}} + P^k_{\mathrm{bat,ch}} + P^k_{\mathrm{HP,heat,el}} + P^k_{\mathrm{HP,cool,el}} + P^k_{\mathrm{grid,exp}}, \tag{17}$$

Here, P^k_{preheat} denotes the additional electrical power demand associated with start-up pre-heating of the electrolyzer and the gas turbine, which is activated during off–on transitions.

Thermal power balance (heating).

$$Q^k_{\mathrm{gt,heat}} + Q^k_{\mathrm{HP,heat}} + Q^k_{\mathrm{TES,dis}} + Q^k_{\mathrm{grid,imp}} = Q^k_{\mathrm{dem}} + Q^k_{\mathrm{TES,ch}} + Q^k_{\mathrm{grid,exp}}. \tag{18}$$

The heat pump is modeled with thermal power as the decision variable, while the corresponding electrical power consumption is imposed by a linear equality constraint:

$$P^k_{\mathrm{HP,heat,el}} = \frac{Q^k_{\mathrm{HP,heat}}}{\mathrm{COP}_{\mathrm{HP,heat}}}. \tag{19}$$

An analogous formulation is applied to cooling, including the corresponding thermal balance, electrical coupling via the energy efficiency ratio (EER), and thermal energy storage.

Storage dynamics (example: BESS).

$$E^{k+1}_{\mathrm{BESS}} = E^k_{\mathrm{BESS}} + \left(\eta_{\mathrm{ch}} P^k_{\mathrm{bat,ch}} - \frac{1}{\eta_{\mathrm{dis}}} P^k_{\mathrm{bat,dis}}\right) \Delta t, \tag{20}$$

$$E_{\mathrm{BESS,min}} \leq E^k_{\mathrm{BESS}} \leq E_{\mathrm{BESS,max}}. \tag{21}$$

Analogous formulations apply to hydrogen storage (HESS) and thermal energy storage (TES). Binary variables enforce mutually exclusive operating modes and unit commitment constraints for the battery, electrolyzer, and gas turbine.

6 Case Setup

6.1 Considered control strategies

Four control strategies are evaluated under identical system conditions to assess the impact of predictive control and forecast accuracy:

- **Case 1 – Rule-Based Control (RB):** Heuristic control with fixed priority rules and no explicit forecasting or optimization.
- **Case 2 – MPC with Seasonal Naive Forecast:** MPC using a 24 h seasonal naive forecast.
- **Case 3 – MPC with LSTM Forecasts:** MPC using LSTM-based forecasts for photovoltaic generation, electrical load, thermal demand, and ambient temperature.
- **Case 4 – MPC with Perfect Forecast:** Idealized MPC with perfect knowledge of all exogenous signals, serving as an upper performance bound.

6.2 System parameters

Table 4 summarizes the parameters used in the MPC–SIM framework. The configuration represents a small-scale, grid-connected P-t-X system with coupled electrical, thermal, and hydrogen subsystems. State-of-charge limits and operational constraints are enforced for all storage components.

The current installation at the Technische Hochschule Ulm includes a 20 kW electrolyzer and a high-pressure hydrogen storage with a capacity of approximately 533 kWh. Since both components are scheduled for expansion, the parameters listed in Table 4 represent an extended configuration to assess future system operation and scalability.

Subsystem	Parameter	Value
BESS	E_{BESS}	[39, 349] kWh
	P_{BESS}	$\pm$194 kW
	η_{BESS}	0.95
H_2 Storage	E_{H2}	[170, 2133] kWh
Electrolyzer	$P_{\text{Ely,el}}$	[32, 80] kW
	$\eta_{\text{Ely,el}}$	piecewise ($\eta_{\max} = 0.60$)
	$T_{\text{Ely,set}}$	60°C
Gas Turbine	$P_{\text{GT,el}}$	[50, 100] kW
	$\eta_{\text{GT,el}}$	piecewise ($\eta_{\max} = 0.32$)
	$\eta_{\text{GT,total}}$	0.90
	$T_{\text{GT,set}}$	600°C
Heat Pump	$P_{\text{HP,el}}$	$\leq$ 50 kW
	COP / EER	4.0/4.0
TES (hot / cold)	E_{TES}	hot: [58,580] kWh cold: [35,350] kWh
	P_{TES}	$\pm$100 kW
	η_{TES}	0.98
Building (3R2C)	R, C, A, f_h	calibrated
	T_{set}	22°C / 24°C

Table 4: Compact overview of system parameters used in the MPC–SIM framework.

7 Results and Discussion

7.1 Annual KPIs

Table 5 summarizes the annual electrical and thermal performance of the investigated control strategies. Electrical performance is assessed using self-consumption and self-sufficiency.

Electrical self-consumption is defined as the ratio of locally generated electricity directly utilized within the system to total local generation,

$$\text{Self-Consumption} = \frac{E_{\text{selfcons,el}}}{E_{\text{local,gen,el}}}, \tag{22}$$

while electrical self-sufficiency denotes the fraction of end-use demand covered by local generation,

$$\text{Self-Sufficiency} = \frac{E_{\text{selfcons}}}{E_{\text{enduse}}}. \tag{23}$$

Overall self-sufficiency is defined analogously and accounts for combined electrical and thermal end-use demand.

Compared to the rule-based reference, all MPC-based strategies significantly increase electrical self-consumption and self-sufficiency.

The MPC with perfect forecasts (MPC-P) achieves the highest values and thus represents an upper performance bound.

Using imperfect forecasts, both the LSTM-based and seasonal naive MPC maintain performance close to this optimum, indicating robust behavior under forecast uncertainty.

In the thermal domain, heating self-sufficiency remains high for all cases, while cooling self-sufficiency is substantially improved by MPC-based operation. Overall, the results confirm that forecast-based MPC consistently enhances electrical and thermal system autonomy without requiring perfect foresight.

7.2 Time series comparison

To complement the annual KPIs, a qualitative comparison of the operational behavior is provided based on exemplary time series of electrolyzer and gas turbine operation. Figures 7 and 8 illustrate the temporal utilization patterns of the different control strategies over the year.

For the rule-based reference, the electrolyzer is predominantly operated during summer periods, while the gas turbine is mainly activated in the morning hours. These patterns reflect the direct response to instantaneous system states and fixed priority rules.

In contrast, all MPC-based strategies result in more structured and temporally coherent operation patterns, reflecting anticipative scheduling and improved coordination between components.

Metric [%]	RB	MPC-P	MPC-LSTM	MPC-SN
Electrical self-consumption	81.39	90.31	89.51	89.37
Electrical self-sufficiency	72.56	76.78	75.77	75.86
Overall self-sufficiency (el+th)	76.37	81.63	80.78	80.79
Thermal self-sufficiency (heating)	99.72	94.75	94.21	94.41
Thermal self-sufficiency (cooling)	54.51	94.34	93.53	92.66

Table 5: Annual electrical and thermal self-sufficiency and self-consumption for the investigated cases.

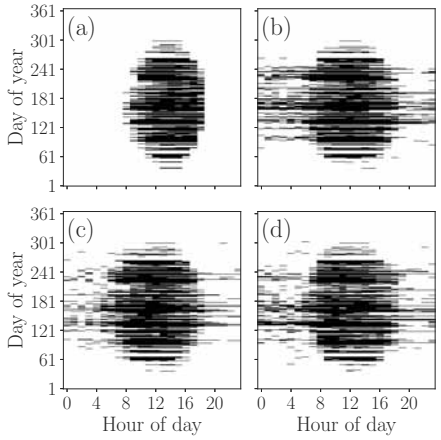

Figure 7: Annual operation patterns of the electrolyzer for the four control strategies: (a) rule-based, (b) MPC-P, (c) MPC-SN, and (d) MPC-LSTM.

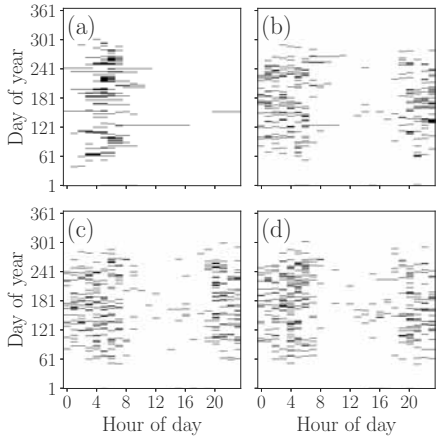

Figure 8: Annual operation patterns of the gas turbine for the four control strategies: (a) rule-based, (b) MPC-P, (c) MPC-SN, and (d) MPC-LSTM.

8 Conclusion and Outlook

This paper presented a forecast-based MPC framework for the operation of a hydrogen-integrated multi-energy system coupled with a dynamic building model. The MPC was formulated as a MILP with an ε-constraint on unit start events and evaluated under different forecast assumptions.

The results show that MPC-based operation consistently outperforms a rule-based reference with respect to electrical and thermal self-sufficiency and self-consumption.

While perfect forecasts yield the highest performance, the use of imperfect forecasts—both LSTM-based and seasonal naive—leads to only marginal reductions. This indicates that the coordinated utilization of flexible components enabled by MPC is more influential than forecast accuracy for the considered setup.

The optimization employs a weighted-sum objective, yielding Pareto-optimal solutions for a given set of weights.

Future work will extend the formulation towards a true multi-objective framework, for example using lexicographic optimization, to systematically explore trade-offs between electrical and thermal objectives.

In addition, the influence of the prediction horizon length on performance and operational behavior will be investigated, particularly with respect to computational effort, forecast uncertainty, and components with slow dynamics.

Further research will address uncertainty-aware optimization and experimental validation of the proposed control framework.

Publication Remark

This contribution is the extended and improved English version of the Workshop Proc. German version for
ASIM Workshop GMMS/STS 2025
Munich/Oberpfaffenhofen 2025,
published in
ASIM Workshop GMMS/STS 2025 Tagungsband
ARGESIM Report 48, e-ISBN 978-3-903347-66-3,
Volume DOI 10.11128/arep.48, p 5-12.

References

[1] Gregor, Liselotte. Hydrogen as an energy carrier for a climate-neutral economy. *EU hydrogen policy*. 2021;.

[2] Kalchschmid V, Erhart V, Angerer K, Roth S, Hohmann A. Decentral Production of Green Hydrogen for Energy Systems: An Economically and Environmentally Viable Solution for Surplus Self-Generated Energy in Manufacturing Companies. *Sustainability*. 2023;15(4).
URL https://www.mdpi.com/2071-1050/15/4/2994

[3] Dominic A, Giliomee J, Zenner T, Winter M, Schullerus G, Booysen M. Green Hydrogen for Future Energy Demand in Germany. In: *2024 IEEE 8th Energy Conference (ENERGYCON)*. 2024; pp. 1–6.

[4] Panagi S, Aresti L, Christodoulides P, Spanias C, Aristidou P. Tuning Performance of Grey-Box Models for Thermal Building Applications. *Preprint*. 2025; Preprint. Available under CC BY 4.0 license.
URL https://doi.org/10.31224/4879

[5] Huang C, Zong Y, You S, Træholt C. Economic model predictive control for multi-energy system considering hydrogen-thermal-electric dynamics and waste heat recovery of MW-level alkaline electrolyzer. *Energy Conversion and Management*. 2022;265:115697.
URL https://www.sciencedirect.com/science/article/pii/S0196890422004939

[6] Zhadan A, Martemyanov A, Allahverdyan A, Petrosian O, Gao H. Linearization Method for MINLP Energy Optimization Problems. *Scientific Reports*. 2025; 15(1):27853.
URL https://doi.org/10.1038/s41598-025-11380-5

[7] Jung M, da Costa Mendes PR, Önnheim M, Gustavsson E. Model Predictive Control when utilizing LSTM as dynamic models. *Engineering Applications of Artificial Intelligence*. 2023;123:106226.
URL https://www.sciencedirect.com/science/article/pii/S0952197623004104

[8] Kreuzer D, Munz M, Schlüter S. Short-term temperature forecasts using a convolutional neural network — An application to different weather stations in Germany. *Machine Learning with Applications*. 2020;2:100007.
URL https://www.sciencedirect.com/science/article/pii/S2666827020300074

[9] Gurobi Optimization, LLC. Gurobi Optimizer Reference Manual. 2024.
URL https://www.gurobi.com

[10] Drgoňa J, Arroyo J, Cupeiro Figueroa I, Blum D, Arendt K, Kim D, Ollé EP, Oravec J, Wetter M, Vrabie DL, Helsen L. All you need to know about model predictive control for buildings. *Annual Reviews in Control*. 2020;50:190–232.
URL https://www.sciencedirect.com/science/article/pii/S1367578820300584